ADVANCED FUNCTIONAL MATERIALS
www.afm-journal.de

Does Electronic Type Matter when Single-Walled Carbon Nanotubes are Used for Electrode Applications?

*G. Dinesha M. R. Dabera, M. R. Ranga Prabhath, Khue T. Lai, K. D. G. Imalka Jayawardena, F. Laurent M. Sam, Lynn J. Rozanski, A. A. Damitha T. Adikaari, and S. Ravi P. Silva**

Single-walled carbon nanotube (SWNT) electrodes that are chemically and mechanically robust are fabricated using a simple drop cast method with thermal annealing and acid treatment. An electronic-type selective decrease in sheet resistance of SWNT electrodes with HNO_3 treatment is shown. Semiconducting SWNTs show a significantly higher affinity toward hole doping in comparison to metallic SWNTs; a ≈12-fold and a ≈fivefold drop in sheet resistance, respectively. The results suggest the insignificance of the electronic type of the SWNTs for the film conductivity after hole doping. The SWNT films have been employed as transparent hole extracting electrodes in bulk heterojunction (BHJ) organic photovoltaics. Performances of the devices enlighten the fact that the electrode film morphology dominates over the electronic type of the doped SWNTs with similar sheet resistance and optical transmission. The power conversion efficiency (PCE) of 4.4% for the best performing device is the best carbon nanotube transparent electrode incorporated large area BHJ solar cell reported to date. This PCE is 90% in terms of PCEs achieved using indium tin oxide (ITO) based reference devices with identical film fabrication parameters indicating the potential of the SWNT electrodes as an ITO replacement toward realization of all carbon solar cells.

1. Introduction

Despite 20 years of discovery single-walled carbon nanotubes (SWNTs) still attract the attention and interest of researchers in many fields due to their outstanding physical, chemical, and electrical properties. A few of the numerous applications of SWNTs are nanoelectronic devices, field emission displays, chemical sensors, actuators, optics, batteries, solar cells, and thin film transistors.[1] The 1D ballistic charge transportation of SWNTs which gives rise to extraordinary electrical conduction is however limited by the inter-nanotube junction contact resistance, intrinsic defects on the nanotube walls, and electron-phonon scattering effects.[2] Hence, the electrical sheet conductivity of SWNT network films is low in reality when compared to the significantly higher conductivity of the constituent SWNTs on their own.

The effect of chemical doping on the enhancement of charge conduction of SWNTs has been widely studied using Bronsted acids, metal chlorides, organometallic compounds, alkali metals, halogens, boron and nitrogen atoms, etc.[3] Among the methods used, acid doping is frequently applied since mere immersion of SWNTs in strong acids (H_2SO_4, HNO_3, and HCl) readily p-dope the SWNTs depending on the strength of the acid used.[4] Hole doping causes a Fermi level (E_F) pinning in the valence band of SWNTs originated by a downshift of the E_F leading to enhanced conductivities through metallization of semiconducting SWNTs (s-SWNTs).[4c,5] Even though, it is known that Bronsted acids p-dope the SWNTs, little has been reported on the selectivity of electronic-type separated SWNTs (s-SWNTs and metallic SWNTs (m-SWNTs)) toward hole doping.

For many years researchers have focused on the replacement of indium tin oxide (ITO) with carbon nanotubes (CNTs) for several reasons. Among the major drawbacks of ITO is its brittleness which limits its use in flexible electronic devices.[6] Another potential shortcoming of ITO usage is the scarcity of indium (In), where its supply is constrained by geo-political and mining issues.[6] This makes ITO expensive since a weight fraction of ≈80%–90% of a typical ITO film constitutes indium. Therefore, carbon being a much cheaper and abundant source makes CNTs a more favored electrode material. Furthermore, the solution processability of CNTs, as opposed to vacuum deposition used for ITO film fabrication, allows the production of large area CNT electrodes using printing techniques. However, there are several limitations of CNTs that need to be addressed prior to large-scale production of solar cells utilizing CNT electrodes. Shorting of the devices due to protruding CNTs, higher roughness of films, and the relatively high sheet resistance are significant obstacles of CNTs compared to ITO films.[6]

In this paper, we discuss the impact of hole doping caused by HNO_3 treatment on electrical conductivities of different

Dr. G. D. M. R. Dabera, M. R. R. Prabhath, Dr. K. T. Lai, Dr. K. D. G. I. Jayawardena, Dr. F. L. M. Sam, Dr. L. J. Rozanski, Dr. A. A. D. T. Adikaari, Prof. S. R. P. Silva
Advanced Technology Institute
University of Surrey
Guildford, Surrey GU2 7XH, UK
E-mail: s.silva@surrey.ac.uk

DOI: 10.1002/adfm.201501394

electronic types of SWNTs. Regioregular poly(3-hexylthiophene-2,5-diyl) (rr-P3HT) wrapped SWNTs (90% s-SWNTs, 90% m-SWNTs, and a mixture of m/s-SWNTs) have been used to fabricate the composite films prior to acid treatment with the formation of well percolated, dispersed networks of SWNTs through polymer wrapping.[7] The original sheet resistance of s-SWNTs, m-SWNTs, and m/s-SWNTs has been significantly reduced by ≈12-fold, ≈eightfold, and ≈fivefold respectively, through the hole doping process. The results suggest that the sheet resistance of the SWNT films (with similar optical transmission) drops to a limiting value irrespective of the electronic type of the SWNTs after acid treatment. The highly conductive doped SWNT thin films have been employed as transparent conductive electrodes in BHJ organic solar cells. Our results indicate that when the conductivity and optical transmission of the doped SWNT electrodes are held constant, the performance of the solar cells is governed by the roughness/morphology of the interface more so than the electronic nature of the SWNTs used. This contradicts the long held belief that m-SWNTs are better for electrode applications considering their lower original sheet resistance. The PCE of 4.4% for the best performing s-SWNT electrode incorporated device is 90% in terms of the PCE of 4.9% for the ITO based reference device with identical film fabrication parameters. To the best of our knowledge, this is the best PCE of a CNT transparent electrode incorporated large area bulk heterojunction (BHJ) solar cell (active area 70 mm^2) reported in the literature.

2. Fabrication of Highly Conductive SWNT Electrodes

rr-P3HT wrapped s-SWNTs, m-SWNTs and a sample of SWNTs containing a mixture of m/s-SWNTs nanotubes in dichlorobenzene (≈0.5 mg mL^{-1}) were used to fabricate semitransparent electrodes. The reason for using a polymer wrapping technique over covalent functionalization is to prevent damage to SWNTs if the latter is used (atomic force microscopic (AFM) images and Raman analysis data are provided in Figures S1 and S2 (Supporting Information), respectively, to prove that the techniques used during the polymer wrapping process do not damage/split the SWNTs). Nanohybrid films were deposited on glass using a simple drop casting process. The solutions were initially drop cast on slightly tilted glass substrates at an angle of ≈45° followed by drying at 40 °C for 10 min allowing the formation of homogeneous uniform films of well-dispersed nanohybrid networks (step 1). The use of a low temperature such as 40 °C prevents coffee staining effects and film shrinking during the drying process. Dried films were subsequently annealed at 300 °C for 5 min, where the wrapped rr-P3HT strands are burnt out while the affinity of the nanotubes to the substrate is drastically improved (step 2). Thermogravimetric analysis (TGA) was performed to estimate the most favorable annealing temperature and 300 °C was found to be the optimum since the polymer burning initiates around 220 °C and structural deformations in s-SWNTs occur if 400 °C is exceeded. (TGA data are given in Figure S3, Supporting Information.) After step 2, the nanotubes from the glass surface cannot be removed by the use of solvents (chlorobenzene, dichlorobenzene, acetone, methanol, water), acids (HNO_3, HCl, H_2SO_4), or wiping off with a tissue. Therefore, this additional step prevents the removal of nanotubes once an acid is introduced. Subsequently, the films were dipped in a 70% HNO_3 solution for 2 h (step 3) to reduce the sheet resistance. The immersion time was selected as 2 h to allow complete intercalation of HNO_3 molecules into the interstitial positions of the SWNT networks.[8]

Based on the TGA measurements, another interesting feature that came into light was that the amount of metallic impurities is significantly reduced during the polymer wrapping process. In Figure S3b (Supporting Information), a residual weight of 29% can be observed which is an indication of the quantity of metal catalysts present from the manufacturing process of 90% s-SWNTs. According to the manufacturer, the metal catalysts present in the sample are nickel, yttrium, and iron. Therefore, the observed residual weight could correspond to nickel and the oxides of yttrium and iron which are readily formed in oxidizing environments. Interestingly, the TGA curve of rr-P3HT/s-SWNT nanohybrids (Figure S3c, Supporting Information) shows a negligible residual weight (<1%) in comparison to 29% in raw s-SWNTs. This indicates that the solvent extraction procedure used during the polymer wrapping process significantly removes the metal impurities of the s-SWNT sample enabling the synthesis of high purity nanohybrids. Hence, it is reasonable to assume that our nanohybrids are free of metal impurities and that the observed phenomena are not due to metallic impurities. Also, if any amorphous carbon is present in the nanohybrids it is believed that these would be removed during the acid soaking process.

AFM images of s-SWNT films during steps 1–3 are given in **Figure 1**a–c, respectively. The average root mean square (RMS) roughnesses of the films are 3.25 ± 0.05, 3.61 ± 0.01, and 3.18 ± 0.14 nm, respectively. The increase in roughness from step 1 to 2 is attributed to the introduction of carbonaceous compounds/impurities resulting from the polymer burning process. The acid soaked film after step 3, has a decreased roughness due to the selective affinity of HNO_3 toward etching carbonaceous compounds that are shelled off from the SWNTs.[9] Therefore, step 3 produces less rough and purer SWNT network films (as will be shown later) and the removal of impurities is visible in the AFM images. An acid soaking method over harsh acid functionalization/oxidation was used to avoid the damage of SWNT walls by strong acids.[10]

Fourier transform IR (FTIR) spectra of the s-SWNT films were obtained to analyze the structural changes introduced during the processes of thermal and acid treatments and the resulting spectra at different wavelength regions are given in Figure 1d–f. FTIR curves denoted as (i) represents a film of pure rr-P3HT, (ii) is a film of pristine s-SWNTs, (iii)–(v) are s-SWNT films after steps 1–3. Figure 1g is the magnified spectrum of (f-(v)) for clarity.

The peaks corresponding to rr-P3HT have disappeared after step 2 indicating the removal of the polymer. The wavelength region 2600–3200 cm^{-1} is magnified in Figure 1e illustrating the three peaks at 2856, 2925, and 2956 cm^{-1} in Figure 1e-(i) resulting from C—H bonds on the aliphatic hexyl chains of rr-P3HT (2856 cm^{-1} = symmetric C—H stretching vibrations of —CH_2—, 2925 and 2956 cm^{-1} = asymmetric C—H stretching vibrations of —CH_2— and —CH_3, respectively).[11] The same

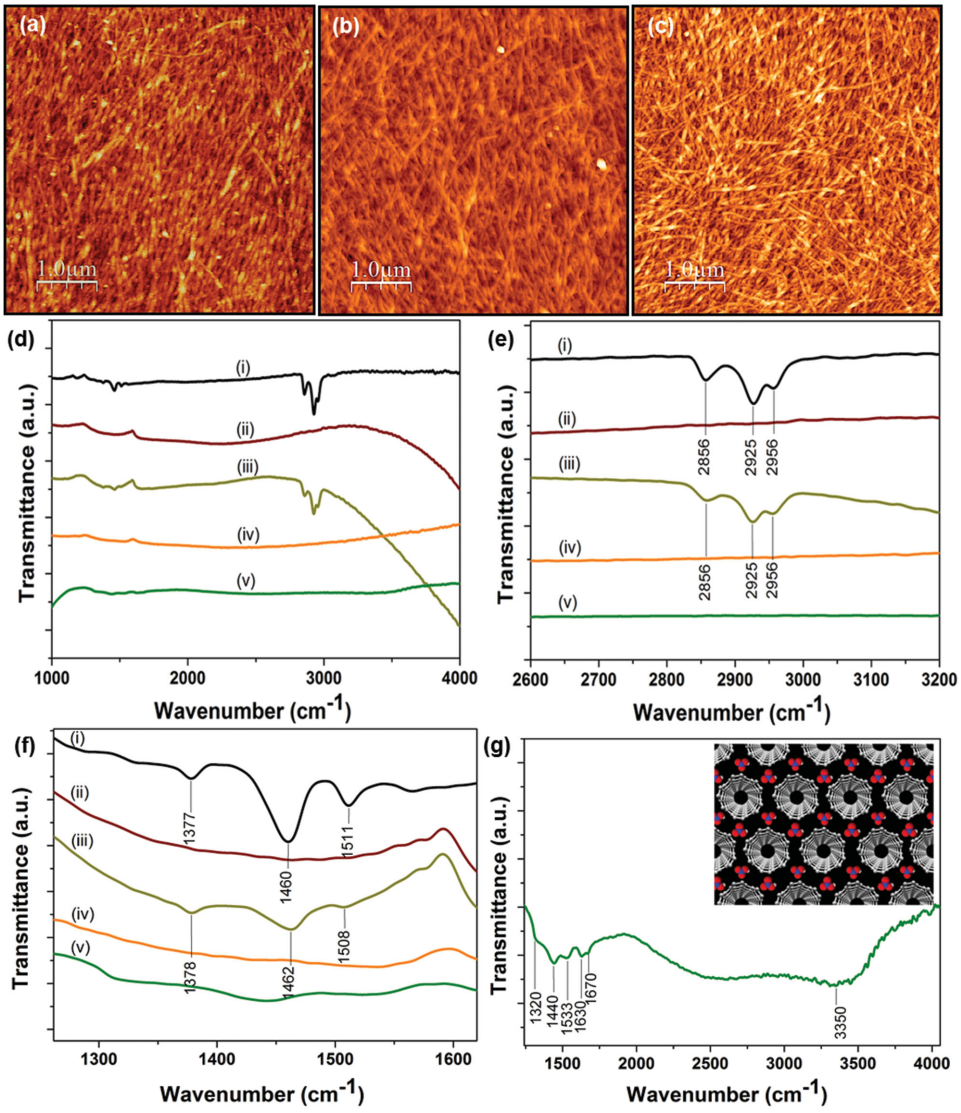

Figure 1. Morphological and chemical changes of SWNT films during electrode fabrication. AFM images of drop cast films of a) rr-P3HT/s-SWNTs (step 1), b) rr-P3HT/s-SWNTs annealed at 300 °C (step 2), and c) rr-P3HT/s-SWNTs soaked in 70% HNO_3 for 2 h (step 3). d–g) FTIR transmittance spectra of s-SWNT films on polished germanium substrates where (i) represents a film of pure rr-P3HT, (ii) is a film of pristine s-SWNTs, (iii)–(v) are s-SWNT films after steps 1–3. d–f) FTIR spectra in different wavelength regions. g) The magnified spectrum of (f-(v)) and the inset is a simple space-filling 3D model illustrating the intercalation of SWNTs by HNO_3 acid. HNO_3 molecules reside in the interstitial positions of an SWNT unit cell where N atoms, O atoms, and H atoms in HNO_3 are represented in blue, red, and gray, respectively.

peaks appear in Figure 1e-(ii) indicating that rr-P3HT is present in the nanohybrid composite films as proven by us previously.[7] There is no sign of the peaks above, corresponding to rr-P3HT in Figure 1e-(iv) which is an indication of absence of rr-P3HT after thermal annealing at 300 °C. The presence of peaks corresponding to rr-P3HT (1377, 1460, and 1511 cm^{-1} are bending vibration modes of —CH_3, symmetric and asymmetric C=C stretching vibrations of the thiophene rings, respectively)[11,12] shown in Figure 1f-(i) and (iii) but not in (iv), further proves the effect of annealing at 300 °C toward complete removal of the polymer. The small variation of the vibration frequencies observed in Figure 1f-(iii) is due to the interactions between the rr-P3HT and s-SWNTs in the nanohybrid composite.[13]

A magnified image of the FTIR spectrum covering the wavelength range 1200–3800 cm^{-1} of the nanotube film soaked in acid (step 3) is given in Figure 1g to analyze the effect of acid treatment on the chemical composition of the SWNTs. The peaks at 1320 and 1670 cm^{-1} are assigned to —NO_2 symmetric and antisymmetric stretching modes while the peak at 1440 cm^{-1} is due to N—OH bending vibrations.[14] The broad peak around 3550 cm^{-1} is attributed to —OH stretching mode and the reasons for the appearance of a broad peak around 2500 cm^{-1} is unclear. This unknown broad feature cannot be due to —OH stretching vibrations of —COOH groups due to the absence of a peak around 1720 cm^{-1} arising from C=O groups.[9] Therefore, this ascertains the fact that HNO_3 treatment does not chemically modify/oxidize the SWNTs (absence

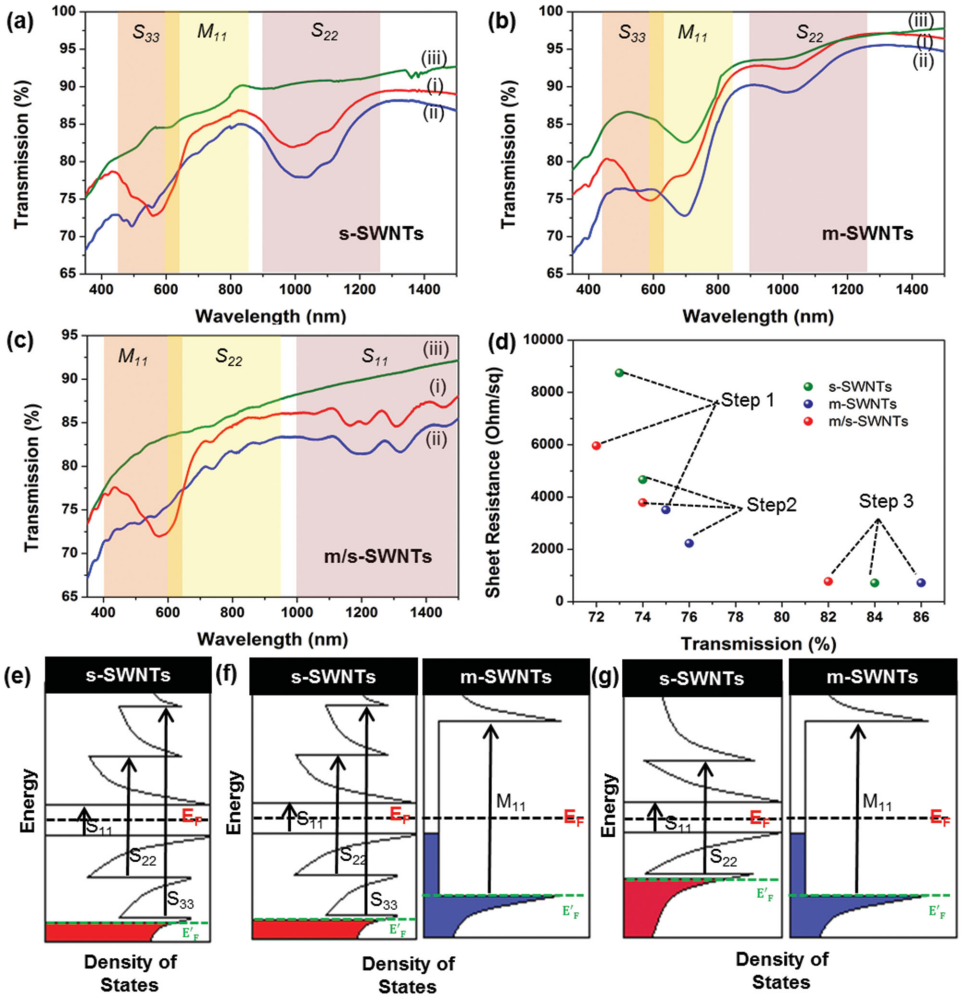

Figure 2. UV–Vis–NIR spectra as proof of SWNT hole doping. a–c) UV–Vis–NIR optical transmission spectra of nanotube films during steps 1–3. Step 1 is the initial drop casting of the rr-P3HT/SWNT films, step 2 is thermal annealing at 300 °C for 5 min, and step 3 is acid soaking of the films in 70% HNO_3 for 2 h. a–c) s-SWNT, m-SWNT, and m/s-SWNT films, respectively. Curves (i), (ii), and (iii) are films after steps 1, 2, and 3. The regions corresponding to VHS transitions are marked based on the diameter of the SWNT type used.[24] The s-SWNTs and m-SWNTs have a diameter distribution in the range of 1.2–1.7 nm, whereas the diameter range of m/s-SWNTs is 0.7–1.4 nm. d) The drop in sheet resistance with increased optical transmission for different types of SWNTs during steps 1–3. e–g) Respective schematic representations of s-SWNTs, m-SWNTs, and m/s-SWNTs after hole doping. First, second, and third VHS transitions of the s-SWNTs are denoted by S_{11}, S_{22}, and S_{33}, whereas the first VHS transition of m-SWNTs is designated as M_{11}. (Note: The m/s-SWNT sample represented in (g) is not a mixture of s-SWNTs and m-SWNTs used in (a) and (b) and is a separate batch of SWNTs from a different supplier.)

of —COOH moieties) as in the case of acid functionalization. The peaks appearing at 1533 and 1630 cm^{-1} correspond to vibrational modes of SWNTs. Bower et al. have shown the action of HNO_3 molecules as intercalants residing in the open channels between the individual SWNTs when exposed to HNO_3.[8] A simple graphical representation of HNO_3 molecules residing in the interstitial positions of an SWNT unit cell is given in Figure 1g, inset.

3. Conductivity Enhancement through Hole Doping

Optical transmission spectra obtained by UV–Vis–NIR spectroscopy (**Figure 2**a–c) further confirms the changes made to the nanohybrid films during steps 1–3. Figure 2a–c corresponds to respective transmission spectra of s-SWNT, m-SWNT, and m/s-SWNT films and curves (i)–(iii) are films after steps 1–3, respectively.

The transmission dip around 570–590 nm in Figure 2a–c-(i) is due to the π–π^* transitions of the wrapped rr-P3HT present in the nanohybrids initially.[7,15] In all three types of films the above transmission dip disappears after step 2 indicating the removal of rr-P3HT from the nanohybrids. The overall transmission decreases after step 2 as a result of the introduction of impurities by the polymer burning process. After step 3, the transmission increases (≈10% at 550 nm) as acid soaking removes the carbonaceous impurities of the films which is desirable for transparent conducting applications.

Table 1. Sheet resistance of SWNT films (12 ± 3 nm) during steps 1–3 with the respective optical transmission values at 550 nm.

Process	s-SWNTs		m-SWNTs		m/s-SWNTs	
	Sheet resistance [Ω □$^{-1}$]	Transmission at 550 nm [%]	Sheet resistance [Ω □$^{-1}$]	Transmission at 550 nm [%]	Sheet resistance [Ω □$^{-1}$]	Transmission at 550 nm [%]
Step 1	8748	73	3509	75	5958	72
Step 2	4669	74	2231	76	3786	74
Step 3	715	84	716	86	769	82

Sheet resistance of the SWNT films during steps 1–3 measured using transmission line method (TLM) and the respective optical transmission of the films at 550 nm are summarized in **Table 1** and are illustrated in Figure 2d. Sheet resistance of SWNT networks depends on two major factors: i) intrinsic resistance of the SWNT type and ii) inter-tube contact resistance.[4b,16] For all three types of films a ≈1.6-fold drop in sheet resistance is observed from step 1 to 2. The similar drop in sheet resistance is attributed to the decrease in contact resistance at the SWNT junctions due to the removal of the surrounding polymer through polymer burning.[4b] However, an interesting pattern in the sheet resistance drop is observed from step 2 to 3 depending on the nature of the SWNT type. The drop in sheet resistance follows the pattern: s-SWNTs > m/s-SWNTs > m-SWNTs with a ≈12, ≈8, and ≈5-fold drop, respectively. The reasons for the above observation are discussed based on doping effects caused by HNO_3 treatment process.

Immersion of SWNT films in Bronsted acids such as HNO_3 and H_2SO_4 has been proven to significantly p-dope individual SWNTs through an effective E_F pinning mechanism inside the valence band as a result of depletion of electrons.[4c,5,17] Thus, the electrical conductivity of doped SWNTs is increased due to the injection of additional mobile holes into the valence band. This phenomenon leads to carrier degeneracy and increase of metallicity of s-SWNTs, enhancing the intrinsic conductivity of s-SWNTs. In addition, in a mixture of s- and m-SWNTs the enhancement of metallicity in s-SWNTs leads to higher conductivities by decreasing the intertube resistance of a semiconducting metallic junction through mitigation of potential Schottky barrier junctions.[4a]

In this work, transitions between Van Hove singularities (VHS) (S_{33}, M_{11}, S_{22}, and S_{11}) observed in transmission spectra of SWNTs (Figure 2a–c) are used to explain the degree of hole doping in the presence of HNO_3.[4b,c,16] Depending on the extent of the downshift of the E_F, M_{11}, S_{22}, and S_{11} transitions in SWNTs should either disappear or suppress due to the depletion of electrons resulting from hole doping. In Figure 2a, both S_{22} and S_{33} transition features are suppressed from step 2 to 3 indicating that the E_F has shifted further down beyond the first, second, and third VHS of the s-SWNTs (Figure 2e). The drastic drop of the E_F accounts for the significant decrease in sheet resistance from step 2 to 3 as a result of increased metallicity of the s-SWNTs.

An important feature of Figure 2b is the peak present at 700 nm due to M_{11} transitions, which is intact from step 2 to 3. This is an indication of the resistance of m-SWNTs toward hole doping. However, a clear decrease in intensity of the peak corresponding to S_{22} is observed (1020 nm) proving that s-SWNTs (present in minute amounts as the sample is 90% m-SWNTs) are more susceptible toward hole doping. Therefore, the least decrease in sheet resistance from step 2 to 3 in m-SWNT sample can be explained through the resistance of m-SWNTs toward hole doping. The observed ≈fivefold decrease in sheet resistance with acid soaking is therefore attributed to doping of s-SWNTs present and the removal of impurities in the m-SWNT film. Considering the increase in S_{22} and S_{33} transition intensities and the unchanged nature of the M_{11} it is believed that the E_F of the doped system lies below the first, second, third VHS of s-SWNTs and above the first VHS of m-SWNTs (Figure 2f).

Figure 2c clearly illustrates the disappearance/heavy suppression of S_{22} and S_{11} transitions from step 2 to 3. Therefore, the estimated E_F of the acid soaked m/s-SWNTs is positioned below the first and second VHS of s-SWNTs (Figure 2g). The ≈eightfold drop in sheet resistance through doping is governed by the enhanced intrinsic conductivity of s-SWNTs and the lowering of the intertube junction resistance between the two types of SWNTs. It should be noted that the difference in the features of Figure 2c in comparison with Figure 2a,b is due to the fact that the m/s-SWNT mixture was purchased from a different supplier (the VHS transitions are dependent on the diameter of the SWNTs used.[24] Both 90% s-SWNTs and 90% m-SWNTs have a diameter distribution in the range of 1.2–1.7 nm whereas the diameter range of the m/s-SWNT sample is 0.7–1.4 nm. Therefore, in addition to the different features of the spectra, the energy regions corresponding to M_{11}, S_{11}, S_{22}, S_{33} transitions in 90% s- and m-SWNT samples are different than that of m/s-SWNT mixture.

In summary, thermal annealing followed by acid soaking drops the original sheet resistance of the SWNT films by ≈12-fold, ≈fivefold, and ≈eightfold for s-SWNTS, m-SWNTs, and m/s-SWNTs, respectively. We note that a similar study has been performed in 2008 by another group[18] which also suggest that m-SWNTs are less susceptible toward hole doping than s-SWNTs.

4. Solar Cells with Doped SWNT Electrodes

The suitability of doped, conductivity-enhanced SWNT films as semitransparent front electrodes in solar cells was studied by fabrication of BHJ devices. Prior to fabrication of solar cells, a thin layer of PEDOT:PSS (EtOH) was spin-coated at 3000 rpm on the doped SWNTs (12 ± 3 nm) with the purpose of reducing the roughness of the films. The RMS roughness of s-SWNT films decreased from 3.18 ± 0.14 to 1.50 ± 0.16 nm and from 3.66 ± 0.01 to 2.26 ± 0.14 nm in m-SWNT films. The layer thickness of PEDOT:PSS (EtOH) used does not completely planarize

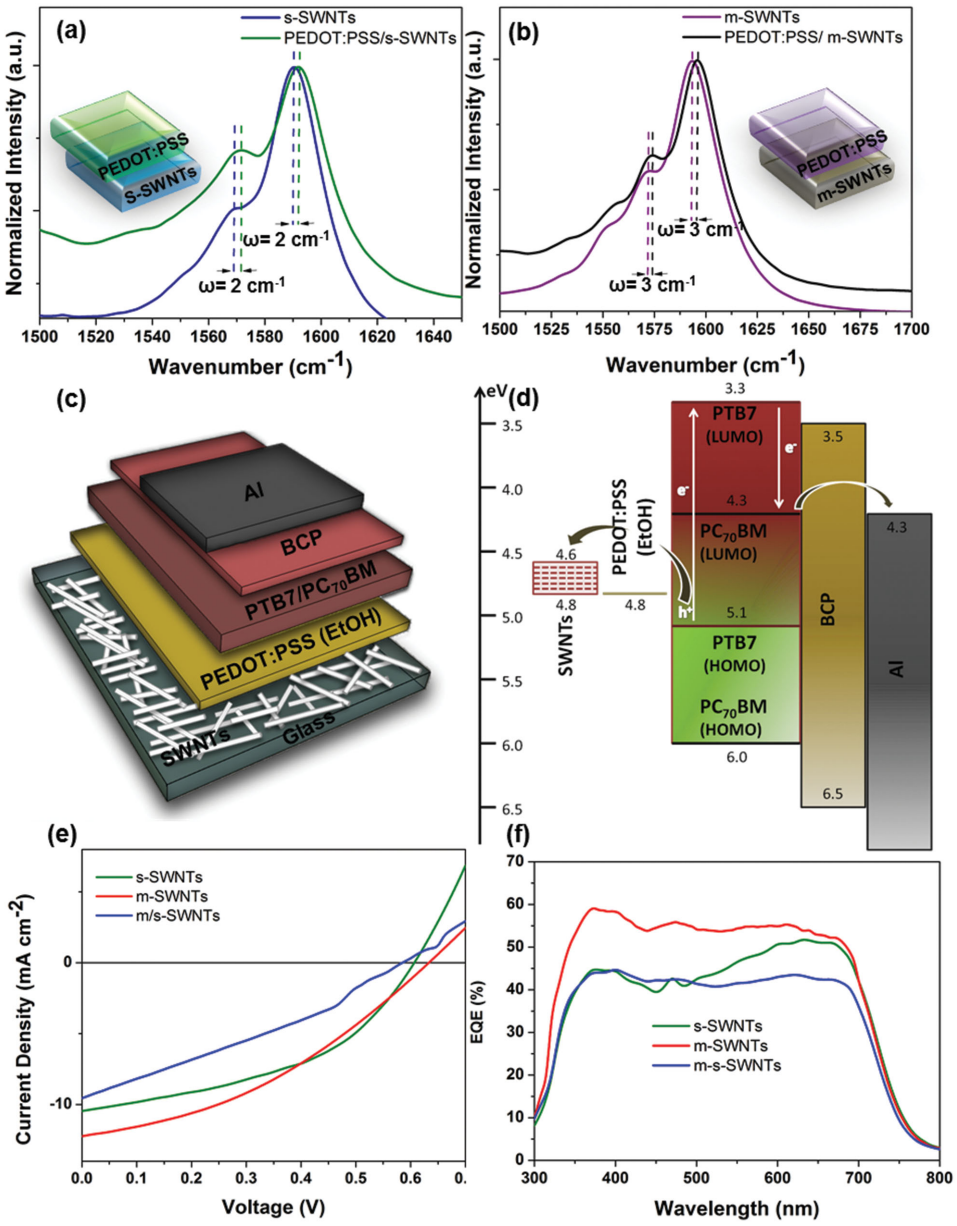

Figure 3. Raman G-band spectra of SWNTs and PEDOT:PSS/SWNT composites. a) G-band spectra of acid treated s-SWNTs and PEDOT:PSS/s-SWNT composite films and b) spectra of acid treated m-SWNTs and PEDOT:PSS/m-SWNT composite films. c) Device architecture and d) the energy level diagram of solar cells utilizing SWNT semitransparent electrodes. e) *J–V* characteristics and f) EQE spectra of the best performing solar cells incorporating single-layered SWNT electrodes and ITO reference electrode. The device architecture is glass/SWNTs or ITO/PEDOT:PSS (EtOH)/PTB7:$PC_{70}BM$/BCP/Al.

the SWNT films although it gives the maximum device performance when employed in devices. In addition, the effect of PEDOT:PSS on the charge transfer process in the device was analyzed using Raman spectroscopy.

Over the years Raman spectroscopy has been used as a tool to study charge transfer processes of CNT composites. According to the literature Raman G-band is sensitive to the charge density of a material hence, a blue (red) shift of the Raman G-band of carbon nanotubes is indicative of the oxidation (reduction) of a species.[19] **Figure 3**a represents the Raman G-band of an acid soaked s-SWNT film (after step 3) (ω_G^+ = 1590 cm^{-1} and ω_G^- = 1569 cm^{-1}) and a composite film of PEDOT:PSS (EtOH) spin-coated on acid treated s-SWNTs (ω_G^+ = 1592 cm^{-1} and ω_G^- = 1571 cm^{-1}). A small blue shift by 2 cm^{-1} in the composite film as compared to pristine acid treated s-SWNTs indicates a doping effect of s-SWNTs by PEDOT:PSS (EtOH). The blue shift is attributed to an oxidation of the s-SWNTs in the presence of PEDOT:PSS (EtOH), leading to a p-doped (oxidized) layer of s-SWNTs. A similar upshift of G-band frequencies is observed when PEDOT:PSS is spin-coated on m-SWNTs (Figure 3b). The G-band blue shifts by 3 cm^{-1} with a ω_G^+ = 1596 cm^{-1} and ω_G^- = 1574 cm^{-1} in PEDOT:PSS/m-SWNTs compared to ω_G^+ = 1593 cm^{-1} and ω_G^- = 1571 cm^{-1} in m-SWNTs.

Table 2. Set 1—Device characteristics of best performing solar cells with doped SWNT electrodes (optical transmission of the s-SWNT, m-SWNT, and m/s-SWNT electrodes at 550 nm are 84%, 86%, and 82%, respectively). Set 2—Device characteristics of best performing solar cells with thicker layers of doped SWNT electrodes (optical transmission of s-SWNT and m-SWNT electrodes at 550 nm ≈72%–73%). The device architecture is glass/SWNTs /PEDOT:PSS (EtOH)/PTB7:$PC_{70}BM$/BCP/Al in both sets.

Electrode type	Electrode sheet resistance [Ω □$^{-1}$]	V_{OC} [V]	J_{SC} (EQE corrected) [mA cm^{-2}]	FF [%]	PCE [%]	R_S [Ω cm^2]	R_{SH} [Ω cm^2]
Set 1 (12 ± 3 nm)							
s-SWNTs	715	0.60	10.47	45.55	2.86	16.8	166.8
m-SWNTs	716	0.64	12.25	36.81	2.89	27.6	178.3
m/s-SWNTs	769	0.58	9.55	30.16	1.67	44.6	72.0
Set 2 (25 ± 5 nm)							
s-SWNTs	187	0.68	12.32	52.14	4.37	15.6	822.2
m-SWNTs	175	0.66	12.84	47.89	4.06	14.6	132.7

The observation of small shifts in wavenumbers are attributed to lower doping concentrations[16] (as a thin layer of PEDOT:PSS is used in devices) and due to the fact that PEDOT:PSS is not covalently attached to the nanotube surface[19] (a physical attachment governed by supramolecular interactions such as van der walls and π–π stacking between the aromatic rings of PEDOT:PSS (EtOH) and SWNTs). The above results suggest an electron transfer from SWNTs to PEDOT:PSS (EtOH) creating slightly oxidized SWNTs and slightly reduced PEDOT:PSS (EtOH) films. This charge transfer process is in favor of solar cell device architecture where an electron transfer from the SWNT electrode to the PEDOT:PSS (EtOH) layer (or a hole transfer from the PEDOT:PSS (EtOH) layer to the CNT electrode) is essential.[20]

Doped SWNT electrode films with characteristics given in Table 1 were used to fabricate solar cells and the devices analyzed are summarized in **Table 2** (set 1). A typical device architecture is; SWNT electrode, a layer of PEDOT:PSS (EtOH), active layer (PTB7:$PC_{70}BM$), a thin layer of bathocuproine (BCP) followed by thermally evaporated aluminium (Figure 3c). Kelvin probe measurements were carried out under ambient conditions to determine the ionization potentials of SWNTs and PEDOT:PSS (EtOH) and are shown in Figure 3d.

PEDOT:PSS (EtOH) was spin-coated at 3000 rpm (60 nm), thickness of the active layer and BCP were 180 and 4 nm, respectively. The current density–voltage (J–V) characteristics of the devices in Table 2 are shown in Figure 3e. The PCEs indicate a similar performance for the s-SWNTs and m-SWNTs whereas the m/s-SWNT electrode gives a poor performance. The short circuit current density (J_{SC}) of m/s-SWNTs is lower than s-SWNTs, though both have an equal optical transmission. The external quantum efficiency (EQE) spectra (Figure 3f) explains the reduction of J_{SC} which is due to high recombination/poor charge collection (further proven by low shunt resistance (R_{SH})) in m/s-SWNT devices. The high series resistance (R_S) in m/s-SWNTs is an indication of a high contact resistance between the PEDOT:PSS and the m/s-SWNTs,[21] the same reason for the reduction of open circuit voltage (V_{oc}).[22] The low R_{SH} of m/s-SWNTs indicates high leakage currents and recombination which could be governed by the morphology of the film.

In order to investigate whether the performance of the devices is controlled by the SWNT electrode morphology/roughness, optical microscopic images (**Figure 4**b,e,h) of the three types of films were taken. The images clearly show the presence of holes/particles of rough nature of the m/s-SWNT films where the purity increases from m-SWNTs to s-SWNTs.

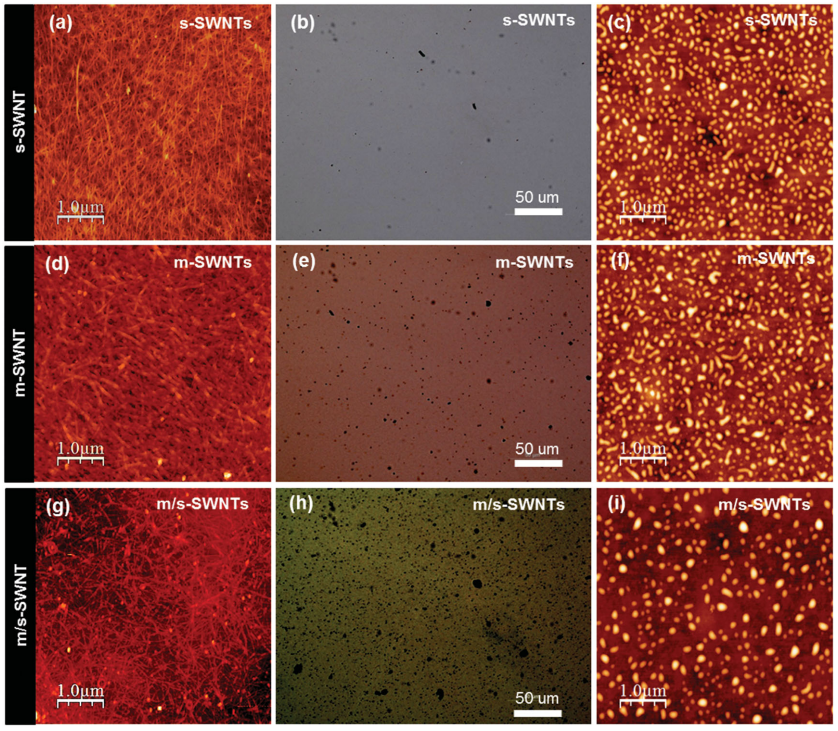

Figure 4. Nanoscale morphology of the SWNT films, the device morphology, and the macroscopic optical images of the SWNT films. a) An AFM image, b) an optical microscopic image of s-SWNTs, and c) an AFM image of the morphology of a device with thermally evaporated BCP on the active layer deposited on SWNT/PEDOT:PSS. Parts (d–(f) and (g)–(i) are the same images using m-SWNTs and m/s-SWNTs, respectively.

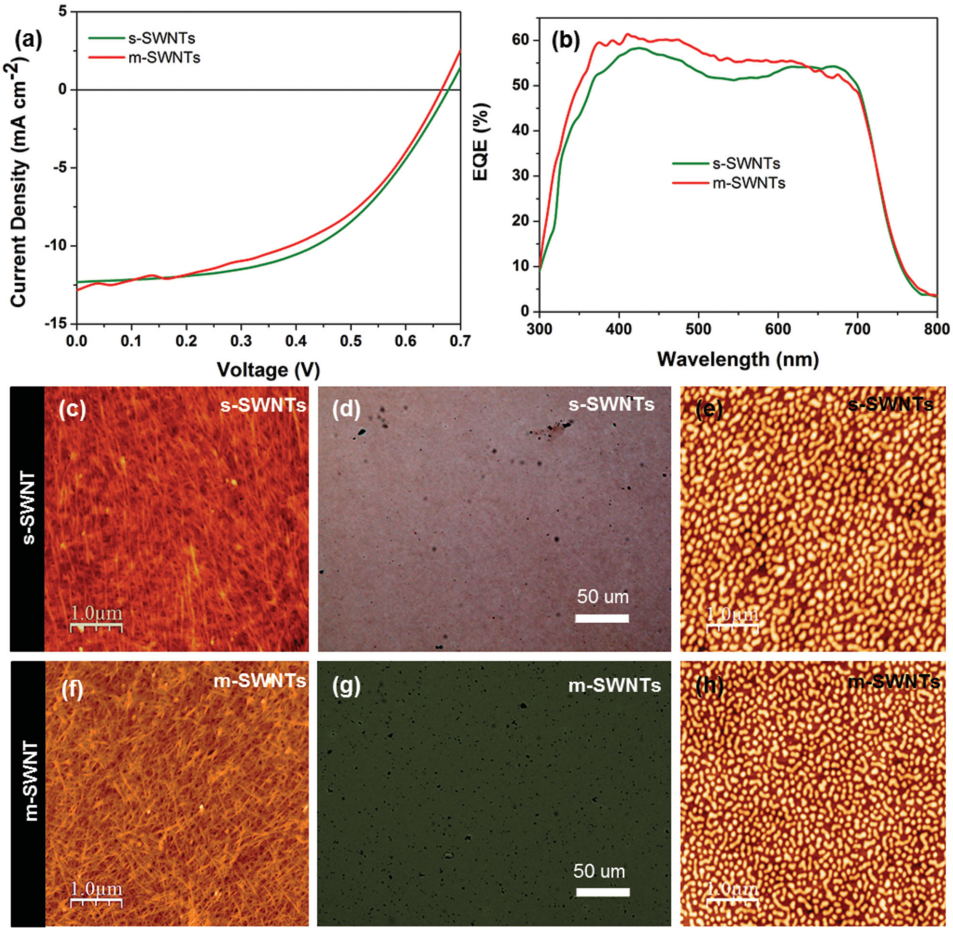

Figure 5. *J–V* characteristics, EQE spectra of devices, and the film morphology. a) *J–V* characteristics of the SWNT-electrode-based devices and b) the respective EQE spectra. The device architecture is glass/SWNTs/PEDOT:PSS (EtOH)/PTB7:$PC_{70}BM$/BCP/Al. c) An AFM image, d) an optical microscopic image of s-SWNTs, and e) an AFM image of the morphology of a device with thermally evaporated BCP on the active layer deposited on SWNT/PEDOT:PSS. Parts (f)–(h) are the same images using m-SWNTs.

In addition, nanoscale particles on the m/s-SWNT layers (Figure 4g) could also be observed from the AFM images which lead to poor device performance.

An interesting feature of the device characteristics is the high J_{SC} of m-SWNT incorporated devices. When comparing the EQE spectra (Figure 3f), the overall EQE is higher for m-SWNTs in comparison to the other two types. The increase in EQE of m-SWNTs due to better charge extraction is omitted as the device R_S is higher. Therefore, the increased EQE and J_{SC} in m-SWNTs are attributed to the higher optical transmission in the wavelength range, 350–1500 nm where m-SWNTs show a transmission around 97%–78% and s-SWNTs in the range of 92%–74% (Figure 2a,b). However, the reduced J_{SC} in s-SWNTs is compensated by the high fill factor (FF) values. This could be explained through the significantly low R_S of the s-SWNTs, whereas the R_{SH} is similar in magnitude for both s-SWNTs and m-SWNTs. Reasons for these variations could range from less resistance between PEDOT:PSS and the s-SWNT electrode, less recombination and the higher roughness of m-SWNTs compared to s-SWNTs.

To further examine the effect of roughness of the SWNT electrode, AFM images of devices after active layer and BCP deposition were obtained. The impact of the roughness of the bottom electrode toward the deposition pattern of the top transport layer (BCP) is clearly visible in Figure 4c,f,i. It is reasonable to state that the formation of the cluster patterns of BCP is templated/affected by the bottom SWNT layers as the only variable in the device architecture is the type of SWNT electrode used. The higher roughness leading to poor device performance of m/s-SWNTs is further reflected through the AFM images showing the separated nature of large BCP clusters in comparison to the other two (a noncontinuous interlayer is detrimental to device performance).

To further increase the device performance by decreasing the sheet resistance, thicker films (25 ± 5 nm) of s-SWNTs and m-SWNTs were fabricated (m/s-SWNTs were not utilized further due to the inherent roughness of the films). The optical transmission of both types of films was maintained around ≈72%–73% at 550 nm. A film of PEDOT:PSS (EtOH) was spin-coated on SWNTs at a spin speed of 3000 rpm (60 nm) and the thickness of the active layer was 180 nm. The thickness of the BCP layer was 4 nm as these device fabrication parameters gave the best performance of the devices. The device performance characteristics are tabulated in Table 2 (set 2) and the corresponding *J–V* curves are shown in **Figure 5**a.

In terms of the PCEs, s-SWNT electrodes perform slightly better in comparison to m-SWNTs. Though the R_S of m-SWNTs is lower than that of s-SWNTs, the FF is dominated by the large increase in R_{SH} in s-SWNTs. The reason is low leakage currents due to smoother/purer s-SWNT films as seen in Figure 5d,g.

The overall EQE (Figure 5b) of m-SWNT device is once again higher than that of s-SWNTs. The increase in EQE of m-SWNT devices due to better charge extraction/less recombination is disregarded as the device R_{SH} is low. In this case, the poor R_{SH} of the device is attributed to the leakage currents due to the presence of particulates/uneven nature of the m-SWNT films as seen in Figure 5d,g optical microscopic images. Therefore, better device performance is expected from m-SWNTs if the leakage currents are reduced.

A reference ITO device fabricated using identical layer thicknesses (PEDOT:PSS spin-coated at 3000 rpm, the active layer PTB7:$PC_{70}BM$ spin-coated at 500 rpm and a 4 nm thick BCP layer) gives a V_{OC} of 0.62 V, J_{SC} of 13.15 mA cm^{-2}, and an FF of 60.10% generating a PCE of 4.9%. In comparison to the ITO based device, the lower J_{SC} observed (for SWNT devices) is due to the lower optical transmission (optical transmission of ITO/glass and SWNT/glass at 550 nm are ≈88% and ≈65%, respectively) and the relatively high sheet resistance of SWNT films (sheet resistance of ITO and SWNTs are ≈15 and ≈175–190 Ω sq^{-1}, respectively). However, it is noted that a J_{SC} in the range of 12.32–12.84 mA cm^{-2} is observed for SWNT incorporated devices (≈94%–98% compared to the J_{SC} of 13.15 mA cm^{-2} for ITO reference), despite the significantly lower optical transmission (≈23% higher optical transmission for ITO) and high sheet resistance (≈12-fold higher for SWNTs) in comparison to ITO electrodes. In addition, it can be seen that the device FF is enhanced by ≈8%–13% when SWNT electrodes are replaced with ITO. We postulate that the reason for the reduced FF values of SWNT incorporated devices is the inherent high roughness of its network in comparison to ITO. Even with the above stated limiting factors of SWNT electrodes, the PCE of the best performing s-SWNT electrode incorporated device (PCE ≈4.4%) is 90% in terms of the PCE achieved using ITO based device with identical film fabrication parameters. Therefore, it is believed that if the optical transmission of the SWNT electrode films are improved further while bringing down the sheet resistance (using more efficient doping agents) and with the use of more effective planarizing layers, the J_{SC} and FF of SWNT devices would be greatly enhanced leading to better device performances which will be better than ITO.

Figure 6 represents the PCEs of BHJ solar cells reported in the literature (from 2005) with CNT electrodes as a replacement for ITO. The PCEs of the devices incorporating CNTs and the reference devices employing ITO reported in each work are tabulated in Table S1 (Supporting Information).

Based on the data shown in Figure 6 (best PCEs of CNT incorporated devices reported in the literature), the PCE of the devices utilizing CNT electrodes are either better or comparable to the best ITO based devices and thus, it is concluded that CNTs could act as an alternative electrode material for ITO. This allows for an alternative to the current technology leader ITO, but is flexible and can be solution processed. However, it should be noted that the reference ITO based devices given in publications are fabricated using identical device fabrication steps (similar thicknesses of the charge extraction and active layers for both types) used in the production of CNT incorporated solar cells.[23] Hence, the reference ITO device in this work was also fabricated with identical layer thicknesses for comparison of our SWNT devices with the values reported in the literature.

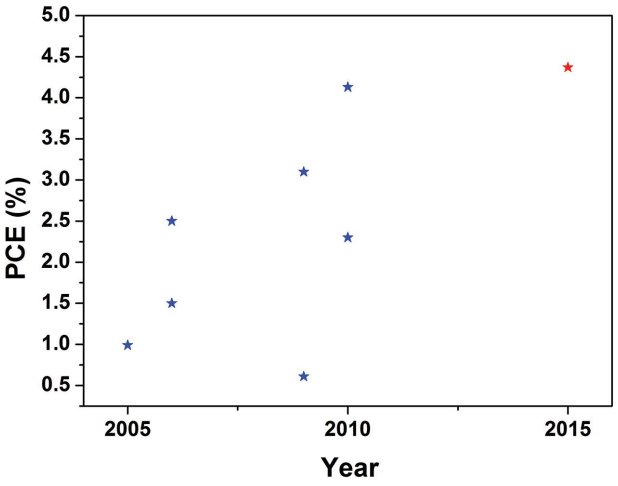

Figure 6. A comparison of champion cell PCE with literature. PCEs of BHJ solar cells utilizing CNTs as the hole collecting electrode reported in the literature.[23a-d,25–27] The point marked with a red star is the maximum PCE of 4.4% reported in this paper.

In comparison to reference devices with similar thicknesses, the devices fabricated in this study, work as good as/better than the work reported in the literature for devices using CNTs as a replacement for ITO. Also, the PCE of 4.4% for the best performing s-SWNT electrode device reported in this work is the best CNT electrode incorporated large area organic BHJ solar cell reported to date. It should be noted that the PCE for optimized ITO based devices (with a similar device architecture but with different film thicknesses) fabricated by us is ≈7.3% (V_{OC} = 0.68 V, J_{SC} = 14.84 mA cm^{-2}, and FF 72.36%). However, the optimized ITO device was not used as the reference device in this work as the purpose of this study was to compare the performance of different electronic types of SWNTs as transparent electrodes in organic photovoltaics (OPVs). Instead, a device with ITO fabricated using similar device fabrication parameters was used here as the reference for comparison with device performance reported in the literature. Therefore, much work should be done in improving the SWNT electrodes to be used as a replacement for ITO electrodes that has been optimized in devices for over several decades.

5. Conclusion

Electronic-type separated s-SWNTs show a higher affinity toward hole doping by HNO_3 in comparison to m-SWNTs. The hole doped SWNT films have been utilized as semitransparent anodic electrodes in BHJ organic solar cells. From our results, it is evident that the electronic type of the acid treated SWNT electrodes does not have an impact on the device performance, and it is the film morphology/roughness that dominate the

device characteristics, provided the sheet resistance and optical transmission of the films are held constant. According to our knowledge, the devices with SWNT electrodes reported in this work are the best CNT electrode incorporated large area BHJ OPVs reported to date. As previously discussed, further work is needed to decrease the transmission of the SWNT layers, increase the conductivity, and to fabricate smoother SWNT layers that will allow the utilization of CNTs as an alternative material for ITO that is not brittle and solution processable.

6. Experimental Section

rr-P3HT Wrapping of SWNTs: rr-P3HT (1.8 mg, Rieke Metals Inc., average molecular weight M_w = 50 000 g mol^{-1} and regioregularity = 95%) was added to chlorobenzene (6 mL) and sonicated for 60 min in an ultrasonic bath. 1.5 mg of SWNTs (i) s-SWNTs/NanointegrisIsoNanotubes-s 90% semiconducting, 10% metallic (composition: 1%–5% carbonaceous impurities and <1% metal impurities), ii) m-SWNTs/NanointegrisIsoNanotubes-m 90% metallic, 10% semiconducting (composition: 1%–5% carbonaceous impurities and <1% metal impurities), and iii) m/s-SWNTs/Sigma-Aldrich single-walled carbon nanotubes (composition: carbon content >90%, carbon as SWNT ≥77%, residual mass <10%)) was added to the solution and was ultrasonically treated for further 60 min. Toluene (2 mL) was added to the solution mixture, sonicated for 15 min, and centrifuged for 8 min at 16 000g in order to remove the excess rr-P3HT in the medium. The precipitate was collected while the supernatant (dark yellow) was discarded. The above sonication and centrifugation procedure was performed twice more and the precipitate was collected while the supernatant (pale yellow) was discarded. The precipitate obtained was dissolved in 1,2-dichlorobenzene (3 mL) by ultrasonication for 60 min such that the final concentration of SWNTs in rr-P3HT/ SWNTs is ≈0.5 mg mL^{-1}.

AFM Imaging: A Veeco dimension 3000 instrument was used for imaging of SWNTs and device active layers. The obtained AFM images were analyzed using WSXM 3.1 software.

FTIR Analysis: A Nicolet 460 Fourier transform infrared spectrometer with a ceramic broadband source, a cesium iodide beam splitter, and a liquid nitrogen cooled mercury cadmium telluride detector was used to measure the transmittance of the samples at 300 K (where transmittance is equal to I/I_o, I is the intensity of the transmitted light through the sample and undoped germanium substrate and I_o is the intensity of the transmitted light through the undoped germanium substrate). The sample compartment was continuously purged with dry nitrogen to reduce absorptions due to atmospheric water vapor and carbon dioxide.

TGA Analysis: TGA analysis was carried out using a TGA Q500 V6.7 Build 203 instrument ramped from room temperature to 800 °C at 10 °C min^{-1} in air.

UV–Vis–NIR: SWNTs were deposited on glass to obtain optical transmission spectra and the glass substrate was considered as the reference sample. Measurements were carried out using a Varian Cary 5000 UV–Vis spectrophotometer.

Sheet Resistance Calculations: TLM was used for sheet resistance calculations and the samples were deposited on glass. Four aluminium (Al) strips with varying distances were thermally evaporated (vacuum of $<3\times10^{-6}$ mbar) on the SWNT films for measurements. A Keithley 4200 was used for current–voltage measurements.

Raman Spectroscopic Analysis: The measurements were carried out using a Renishaw micro-Raman system with an Ar^+ laser operating at a wavelength of 514.5 nm (green).

Kelvin Probe Measurements: Anfatec ambient single-point Kelvin probe system was used for measurements.

OPV Fabrication and Measurements: SWNT Electrode Deposition: s-SWNTs, m-SWNTs, and m/s-SWNTs were drop cast on slanted glass so that the excess solution drained away to obtain uniform films. The films were then slow annealed at 40 °C until dry (10 min) to avoid sudden film shrinking at higher temperatures—step 1. The dried films were annealed at 300 °C for 3 min to remove the surrounding rr-P3HT—step 2. Annealed films were then soaked in 70% HNO_3 for 2 h in order to remove the carbonaceous impurities and to further enhance the conductivity—step 3.

PEDOT:PSS (EtOH): EtOH (1 mL) was added to PEDOT:PSS (4 mL, Baytron PVP AI 4083) in order to increase the wetting properties of PEDOT:PSS on SWNTs.

PTB7/PC70BM Active Layer: PTB7 (10 mg, 1-material Chemscitech Inc.) and $PC_{70}BM$ (15 mg, 99% pure, Solenne) were added to a solvent mixture of chlorobenzene/1,8-diiodooctane (97:3 vol%, total volume 1 mL) and the solution was stirred for one week prior to filtering of the solution using a 0.2 µm filter.

Table 2/Set 1: Glass which had been cleaned in an ultrasonic bath using Decon-90, deionized water, acetone, and methanol was subjected to an oxygen plasma treatment for 5 min prior to deposition of the SWNT films. Three types of SWNT films after step 3 were used as transparent electrodes and PEDOT:PSS (EtOH) was spin-coated at 3000 rpm for 40 s followed by thermal annealing at 155 °C for 10 min. A two-step spin-coating process was used for the spin-coating of the active layer; first step at 500 rpm for 2 min and second step at 1500 rpm for 2 s, which was found to yield optimal device performance.

ITO Reference Device: PEDOT:PSS (EtOH) was spin-coated at 3000 rpm for 40 s and thermally annealed at 155 °C for 10 min on cleaned ITO glass (same cleaning procedure as above). The active layer consisting of PTB7/$PC_{70}BM$ was spin-coated using a two-step process: first step at a spin speed of 500 rpm for 2 min and a second step at 1500 rpm for 2 s.

Optimized ITO Device: PEDOT:PSS (EtOH) was spin-coated at 5000 rpm for 40 s and thermally annealed at 155 °C for 10 min on cleaned ITO glass (same cleaning procedure as above). The active layer consisting of PTB7/$PC_{70}BM$ was spin-coated at a spin speed of 1000 rpm for 2 min. The spin-coated devices were allowed to dry slowly in closed Petri dishes (60 mm diameter, 15 mm height) at room temperature for 1.5 h. The hole blocking layer, BCP (4 nm) and Al (40 nm) electrode (cathode) were then thermally evaporated under vacuum of $<3\times10^{-6}$ mbar. All the steps involved in device fabrication were carried out in a nitrogen filled MBRAUN glove box. Current density–voltage (J–V) measurements were performed using a Keithley 2400 exposing the devices to stimulated AM 1.5G light (obtained from 300 W Xe Arc lamp ORIEL simulator calibrated to an intensity of 1000 W m^{-2} with a Newport reference solar cell) at room temperature.

Table 2/Set 2: Two layers of s-SWNT and m-SWNT films were used as the electrodes. Deposition of the second layer of SWNTs were carried out after performing step 2 to avoid removal of the bottom layer by the subsequent layer as a result of common solvents used (dichlorobenzene). PEDOT:PSS (EtOH) was spin-coated at a speed of 3000 rpm for 40 s and was annealed at a temperature of 155 °C for 10 min. The active layer consisting of PTB7/$PC_{70}BM$ was spin-coated at 500 rpm for 2 min followed by 1500 rpm for 2 s. All devices were slow dried for 1.5 h at room temperature. The hole blocking layer, BCP (4 nm) and Al (40 nm) electrode (cathode) were then thermally evaporated under vacuum of $<3\times10^{-6}$ mbar. All the steps involved in device fabrication were carried out in a nitrogen filled MBRAUN glove box. The active area of all OPV devices were 70 mm^2. Current density–voltage (J–V) measurements were performed using a Keithley 2400 exposing the devices to stimulated AM 1.5G light (obtained from Abet Technologies-10500 solar simulator calibrated to an intensity of 1000 W m^{-2} with a Newport reference solar cell) at room temperature.

EQE Measurements: Measurements of EQE were carried out using a Bentham PV300 photovoltaic device characterization system, under a bias of 1 sun obtained from a halogen lamp.

Supporting Information

Supporting Information is available from the Wiley Online Library or from the author.

Acknowledgements

G.D.M.R.D. acknowledges support from the Overseas Research Scholarship/University Research Scholarship–University of Surrey. The authors would like to thank R. Gwilliam and M. A. Razali for the supply and cleaning of the undoped germanium substrates for the optical measurements and V. Doukova for the assistance with TGA measurements.

Received: April 7, 2015
Revised: May 11, 2015
Published online: June 15, 2015

[1] P. Ajayan, O. Zhou, in *Carbon Nanotubes* Vol. *80* (Eds: M. Dresselhaus, G. Dresselhaus, P. Avouris), Springer, Berlin **2001**, p 391.
[2] a) K. D. G. I. Jayawardena, L. J. Rozanski, C. A. Mills, M. J. Beliatis, N. A. Nismy, S. R. P. Silva, *Nanoscale* **2013**, *5*, 8411; b) M. Biercuk, S. Ilani, C. Marcus, P. McEuen, in *Carbon Nanotubes* Vol. *111*, Springer, Berlin **2008**, p 455.
[3] a) V. K. Marianne Glerup, C. Ewels, M. Holzinger, G. Van Lier, in *Doping of Carbon Nanotubes, Doped Nanomaterials and Nanodevices* Vol. *3* (Ed: W. Chen), American Scientific Publishers, California **2010**; b) H. Shiozawa, T. Pichler, C. Kramberger, M. Rümmeli, D. Batchelor, Z. Liu, K. Suenaga, H. Kataura, S. R. P. Silva, *Phys. Rev. Lett.* **2009**, *102*, 046804.
[4] a) R. Jackson, B. Domercq, R. Jain, B. Kippelen, S. Graham, *Adv. Funct. Mater.* **2008**, *18*, 2548; b) S. Dong-Wook, L. J. Hak, K. Yu-Hee, Y. S. Man, P. Seong-Yong, Y. Ji-Beom, *Nanotechnology* **2009**, *20*, 475703; c) W. Zhou, J. Vavro, N. M. Nemes, J. E. Fischer, F. Borondics, K. Kamarás, D. B. Tanner, *Phys. Rev. B* **2005**, *71*, 205423.
[5] a) F. Hennrich, R. Wellmann, S. Malik, S. Lebedkin, M. M. Kappes, *Phys. Chem. Chem. Phys.* **2003**, *5*, 178; b) J. G. Coroneus, B. R. Goldsmith, J. A. Lamboy, A. A. Kane, P. G. Collins, G. A. Weiss, *ChemPhysChem* **2008**, *9*, 1053.
[6] J. Sun, R. Wang, in *Carbon Nanotube Transparent Electrode: Syntheses and Applications of Carbon Nanotubes and Their Composites* (Ed: S. Suzuki), InTech, Croatia **2013**, Ch. 14.
[7] G. D. M. R. Dabera, K. D. G. I. Jayawardena, M. R. R. Prabhath, I. Yahya, Y. Y. Tan, N. A. Nismy, H. Shiozawa, M. Sauer, G. Ruiz-Soria, P. Ayala, V. Stolojan, A. A. D. T. Adikaari, P. D. Jarowski, T. Pichler, S. R. P. Silva, *ACS Nano* **2012**, *7*, 556.
[8] C. Bower, A. Kleinhammes, Y. Wu, O. Zhou, *Chem. Phys. Lett.* **1998**, *288*, 481.
[9] J. Zhang, H. Zou, Q. Qing, Y. Yang, Q. Li, Z. Liu, X. Guo, Z. Du, *J. Phys. Chem. B* **2003**, *107*, 3712.
[10] N. A. Nismy, A. A. D. T. Adikaari, S. R. P. Silva, *Appl. Phys. Lett.* **2010**, *97*, 033105.
[11] H. Wei, L. Scudiero, H. Eilers, *Appl. Surf. Sci.* **2009**, *255*, 8593.
[12] Y. Du, S. Z. Shen, W. D. Yang, K. F. Cai, P. S. Casey, *Synth. Met.* **2012**, *162*, 375.
[13] R. Koizhaiganova, H. J. Kim, T. Vasudevan, S. Kudaibergenov, M. S. Lee, *J. Appl. Polym. Sci.* **2010**, *115*, 2448.
[14] I. K. Ortega, R. Escribano, D. Fernandez, V. J. Herrero, B. Mate, A. Medialdea, M. A. Moreno, *Chem. Phys. Lett.* **2003**, *378*, 218.
[15] T. Schuettfort, H. J. Snaith, A. Nish, R. J. Nicholas, *Nanotechnology* **2010**, *21*, 025201.
[16] K. K. Kim, J. J. Bae, H. K. Park, S. M. Kim, H.-Z. Geng, K. A. Park, H.-J. Shin, S.-M. Yoon, A. Benayad, J.-Y. Choi, Y. H. Lee, *J. Am. Chem. Soc.* **2008**, *130*, 12757.
[17] Y. Miyata, Y. Maniwa, H. Kataura, *J. Phys. Chem. B* **2005**, *110*, 25.
[18] a) J. L. Blackburn, T. M. Barnes, M. C. Beard, Y.-H. Kim, R. C. Tenent, T. J. McDonald, B. To, T. J. Coutts, M. J. Heben, *ACS Nano* **2008**, *2*, 1266; b) T. M. Barnes, J. L. Blackburn, J. van de Lagemaat, T. J. Coutts, M. J. Heben, *ACS Nano* **2008**, *2*, 1968.
[19] A. M. Rao, P. C. Eklund, S. Bandow, A. Thess, R. E. Smalley, *Nature* **1997**, *388*, 257.
[20] H. Park, S. Chang, J. Jean, J. J. Cheng, P. T. Araujo, M. Wang, M. G. Bawendi, M. S. Dresselhaus, V. Bulović, J. Kong, S. Gradečak, *Nano Lett.* **2012**, *13*, 233.
[21] A. Guerrero, T. Ripolles-Sanchis, P. P. Boix, G. Garcia-Belmonte, *Org. Electron.* **2012**, *13*, 2326.
[22] B. Qi, J. Wang, *J. Mater. Chem.* **2012**, *22*, 24315.
[23] a) A. D. Pasquier, H. E. Unalan, A. Kanwal, S. Miller, M. Chhowalla, *Appl. Phys. Lett.* **2005**, *87*, 203511; b) J. van de Lagemaat, T. M. Barnes, G. Rumbles, S. E. Shaheen, T. J. Coutts, C. Weeks, I. Levitsky, J. Peltola, P. Glatkowski, *Appl. Phys. Lett.* **2006**, *88*, 233503; c) Y. Feng, X. Ju, W. Feng, H. Zhang, Y. Cheng, J. Liu, A. Fujii, M. Ozaki, K. Yoshino, *Appl. Phys. Lett.* **2009**, *94*, 123302; d) T. M. Barnes, J. D. Bergeson, R. C. Tenent, B. A. Larsen, G. Teeter, K. M. Jones, J. L. Blackburn, J. van de Lagemaat, *Appl. Phys. Lett.* **2010**, *96*, 243309.
[24] H. Kataura, Y. Kumazawa, Y. Maniwa, I. Umezu, S. Suzuki, Y. Ohtsuka, Y. Achiba, *Synth. Met.* **1999**, *103*, 2555.
[25] M. W. Rowell, M. A. Topinka, M. D. McGehee, H.-J. Prall, G. Dennler, N. S. Sariciftci, L. Hu, G. Gruner, *Appl. Phys. Lett.* **2006**, *88*, 233506.
[26] R. C. Tenent, T. M. Barnes, J. D. Bergeson, A. J. Ferguson, B. To, L. M. Gedvilas, M. J. Heben, J. L. Blackburn, *Adv. Mater.* **2009**, *21*, 3210.
[27] S. Kim, J. Yim, X. Wang, D. D. C. Bradley, S. Lee, J. C. deMello, *Adv. Funct. Mater.* **2010**, *20*, 2310.